AFRL-RW-EG-TR-2011-126

Explosively Driven Particle Fields Imaged Using a High-Speed Framing Camera and Particle Image Velocimetry

Charles M. Jenkins
Yasuyuki Horie

Air Force Research Laboratory
Munitions Directorate/Ordnance Division
Energetic Materials Branch (AFRL/RWME)
Eglin AFB,FL 32542-5910

Robert C. Ripley

Martec Limited
1888 Brunswick Street
Halifax, NS, B3J3J8, Canada

William H. Wilson

Defense Threat Reduction Agency
8725 John J. Kingman Road
Fort Belvoir, VA 22060-6201

August 2011

Final Report

AIR FORCE RESEARCH LABORATORY, MUNITIONS DIRECTORATE

Air Force Materiel Command ■ United States Air Force ■ Eglin Air Force Base

NOTICE AND SIGNATURE PAGE

Qualified requestors may obtain copies of this report from the Defense Technical Information Center (DTIC) (http://www.dtic.mil).

AFRL-RW-EG-TR-2011-126 HAS BEEN REVIEWED AND IS APPROVED FOR PUBLICATION IN ACCORDANCE WITH ASSIGNED DISTRIBUTION STATEMENT.

FOR THE DIRECTOR:

//ORIGINAL SIGNED//   //ORIGINAL SIGNED//   //ORIGINAL SIGNED//

HOWARD G. WHITE, PhD   JENNIFER L. JORDAN, PhD   CHARLES M. JENKINS
Technical Advisor   Technical Advisor   Project Manager
Ordnance Division   Energetic Materials Branch   Energetic Materials Branch

This page intentionally left blank

REPORT DOCUMENTATION PAGE

1. REPORT DATE *(DD-MM-YYYY)* 08-2011	2. REPORT TYPE Final	3. DATES COVERED *(From - To)* 14 February 2008 – 1 August 2011

4. TITLE AND SUBTITLE

Explosively Driven Particle Fields Imaged Using a High-Speed Framing Camera and Particle Image Velocimetry

5a. CONTRACT NUMBER

5b. GRANT NUMBER

5c. PROGRAM ELEMENT NUMBER
00000D

6. AUTHOR(S)

Charles M. Jenkins, Yasuyuki Horie, Robert C. Ripley, William H. Wilson

5d. PROJECT NUMBER
DTRN

5e. TASK NUMBER
M8

5f. WORK UNIT NUMBER
05

7. PERFORMING ORGANIZATION NAME(S) AND ADDRESS(ES)

Air Force Research Laboratory, Munitions Directorate
Ordnance Division
Energetic Materials Branch (AFRL/RWME)
Eglin AFB FL 32542-5910

8. PERFORMING ORGANIZATION REPORT NUMBER

AFRL-RW-EG-TR-2011-126

9. SPONSORING / MONITORING AGENCY NAME(S) AND ADDRESS(ES)

Air Force Research Laboratory, Munitions Directorate
Ordnance Division
Energetic Materials Branch (AFRL/RWME)
Eglin AFB FL 32542-5910
Technical Advisor: Dr. Jennifer Jordan

10. SPONSOR/MONITOR'S ACRONYM(S)

AFRL-RW-EG

11. SPONSOR/MONITOR'S REPORT NUMBER(S)
AFRL-RW-EG-TR-2011-126

12. DISTRIBUTION / AVAILABILITY STATEMENT

Distribution A: Approved for public release; distribution unlimited. Approval Confirmation 96 ABW/PA # 96ABW-2011-0255, dated May 25, 2011

13. SUPPLEMENTARY NOTES   SUBJECT TO EXPORT CONTROL LAWS
DISTRIBUTION STATEMENT INDICATING AUTHORIZED ACCESS IS ON THE COVER PAGE AND BLOCK 12 OF THIS FORM.
DATA RIGHTS RESTRICTIONS AND AVAILABILITY OF THIS REPORT ARE SHOWN ON THE NOTICE AND SIGNATURE PAGE.

14. ABSTRACT

Metallic particles have been an ingredient in high explosives for decades due to their large energy release upon combustion. A concern over the understanding of metal particle combustion release rates has driven the development of simulation packages for detonation and blast-wave dynamics. The current models for metallic particles are a primary source of error in simulations and require experimental data to adjust them. This effort provided experimental data using two existing methods, particle image velocimetry and a high speed framing camera to determine the particle speed and concentration within blast waves of different mean particle sizes of aluminum and tungsten powder. The numerical model Chinook was used to estimate particle velocity, concentration and arrival times at the point where the experimental measurements were recorded. Estimates of particle drag coefficients and were also compared to the numerical model as well as particle and shock interactions.

15. SUBJECT TERMS
Blastwave imaging, multi-phase flow, PIV

16. SECURITY CLASSIFICATION OF:			17. LIMITATION OF ABSTRACT	18. NUMBER OF PAGES	19a. NAME OF RESPONSIBLE PERSON Charles M. Jenkins
a. REPORT UNCLASSIFIED	**b. ABSTRACT** UNCLASSIFIED	**c. THIS PAGE** UNCLASSIFIED	SAR	33	**19b. TELEPHONE NUMBER** *(include area code)* 850-882-5902

This page intentionally left blank

TABLE OF CONTENTS

LIST OF FIGURES

LIST OF TABLES

1. INTRODUCTION

Detonation of a heterogeneous explosive provides momentum and energy transfer from the explosive to the solid particles within or packed around the outer shell of the explosive medium. The particles become accelerated by the initial shock wave from the explosive and its rapidly expanding product generates a two-phase flow into the surrounding environment. If the explosive contains metallic particles which are reactive under high temperature and pressure and they have the correct morphology, ignition of the particles may take place if oxidizing gases are present (Frost *et al.* 2007). However, if inert particles are used in the explosive or ignitions of the reactive particles are delayed sufficiently until the particle number falls to a low count, the energy release will not add to the blast wave (Frost *et al.* 2007). Experimental studies have been conducted by Zhang *et al.* (2001) and Frost *et al.* (2007) using inert steel particles and by Frost *et al.* (2005, 2007) with reactive aluminum and magnesium particles. All used sensitized nitromethane and were compared with numerical predictions.

In addition to particle collisions, particles are thought to have significant influence on shock transmission and the resulting compressive heating of gas and particles. The combination of experimental data with numerical simulations yields a greater understanding of particle and shock interaction in gaseous media. Numerical shock wave investigations of this type have been reviewed by Saito *et al.* (2003), Zhang *et al.* (2003), Engelhardt (2008), Donahue *et al.* (2007) and Dunbar *et al.* (2011) for modeling specific to this research. An additional review of momentum transfer due to the interaction of shock waves with solid particles was reviewed by Zhang *et al.* (2003) where the relationships of particle shock interaction time and velocity relaxation time was described. These phenomena occur when the particle crosses the shock front and the ratio of the particle interaction time to the particle velocity relaxation time provides a criterion for determining whether a change in the particle velocity is significant due to the shock interaction. Accurate measurement of particle velocity is therefore critical to assess momentum and energy transfer from the gas medium to the solid particle phase. Despite the use of high speed cameras and other image based methods, Frost and Zhang (2006) stated that currently challenges remain related to the development of robust in situ diagnostics for probing the flow parameters such as particle and gas temperature, pressure, particle density, and velocity within the multiphase fireball because of the complexities of the particle field.

In studies cited earlier, methods used to collect velocity and impulse data included flash x-ray, high speed video, momentum traps, blast pressure "lollipop" gauges and particle streak gauges. These techniques for the most part average small areas of the blast wave which may contain a heterogeneous distribution of particles. These techniques have traditionally not provided information specific to individual or small groups of 10-15 particles. Particle image velocimetry (PIV) has the ability to provide information specific to individual particles when the flow field has low image densities and in regions of higher image density a resultant velocity vector for small groups of particles is provided. PIV is capable of providing information on particle position, size, velocity and concentration under certain conditions. Published work has demonstrated the feasibility of performing PIV measurements in the hot, high-speed exhaust plume of a solid rocket motor using natural occurring particles (Balakumar and Adrian, 2004). For short duration events, PIV has also been demonstrated that dispersed olive oil droplets using an exploding bridge wire can be imaged and velocities determined (Murphy *et al.*, 2005). The

1

application of PIV to image and track particle fields driven by a core of high explosive has also been reported by Jenkins *et al.* (2010).

Small scale testing of explosively loaded items have become experimentally attractive because of the high cost associated with testing large items and the ability to provide larger numbers of test items for greater confidence in statistical evaluations. Gagliardi et al. (2005) noted that small-scale tests are initially used to obtain a useful amount of data from a small amount of explosives, considering safety, cost, and speed of production and that small-scale testing is very useful. Information on scalability of small charges, particle turbulence and dispersal are also of interest for enhancement of numeric models.

The study described herein uses displacement data from a high speed framing camera (HSFC) and a PIV instrument for determining particle field velocities. The primary objective of the study was to improve the measurement accuracy of particle velocity and position in support of numerical models. A second objective was to provide imagery of the blast wave to aid in identifying particle interactions such as clustering and particle flow field shape with changes in particle shape.

2. EXPERIMENTAL SETUP AND METHODOLOGY

The basic set-up (Figure 1) was the same as that reported by Jenkins *et al.* (2010) using the same PIV instrumentation and test support equipment with a few exceptions identified in this study. The optics box, laser and camera portal windows for this study were made from 0.5 inch sapphire material with an anti-reflective coating provided by Crystal Systems Inc. These windows were produced by the heat exchanger method (HEM) and had a 60/40 polished surface quality on the faces and a surface peak to valley (PV) flatness better than 2λ at 633 nm. The material and coating was specified to reduce the energy reflectance at 532 nm from 5 percent per interface determined with BK-7 glass, used in previous reported tests (Jenkins *et al.* 2010), to less than 0.25 per interface. Optical flatness and parallelism was improved to less than 5 arc minutes due to the increased flatness of the sapphire.

Hot aluminum and tungsten particles are broad band emitters that emit 532 nm light. A filter stack was used to remove all frequencies except 532 ± 2 nm light and to reduce luminosity across the remaining spectrum from the burning and hot particles; this helped prevent over saturation of the imaging chip. The reduction in light transmission was between 50 percent and 55 percent through each filter in the stack. The filter stack was varied between 2-3 filters depending on the expected brightness of the test event. The camera was fitted with a 105 mm Nikkor lens (Model No. 610044) made by Nikon and set at an *f*-number = 4.5. The *f*-number was reduced from previous work in order to decrease the depth of field and reduce the number of ghost images produced from the hot particles. These images were outside of the light sheet but within the depth of field of the lens. The standoff distance from the light sheet to the surface of the outer lens was 81.3 cm (32 inches) making the magnification 0.1 M. This distance was checked after each test for movement of the light box and test stand positions after each shot.

The test items contained a core of organic explosive made from four stacked ½ x ½ inch cylindrical pressed pellets, pressed to 90 percent theoretic maximum density (crystal density) and

2

glued together into a single 5.08 cm stick. The explosive composition consists of 95.3 percent octahydro-1,3,5,7-tetranitro-1,3,5,7-tetrazocane (HMX) and 4.7 percent binder to ensure dimensional stability.

Metallic powders were used to fill the annular space between the wall of a paper tube and the HMX core. These particles acted as the natural tracer particles for PIV tracking. The aluminum powders H-10 (d_p = 13.4 µm) and H-95 (d_p = 113.4 µm) were used along with charges containing the tungsten powder W-27 (d_p= 34.5 µm) as a comparison to the known lower density and reactive aluminum powders. The particle size distributions (PSD) were determined using a laser diffraction particle analyzer (LS13320, produced by Beckman-Coulter). All powder charges were filled to their tap density (Table 1). To provide a baseline for comparison with the powder charges, a solid aluminum shell case made of 6061-T6 wall thickness of 3.2 mm was tested.

Initial particle expansion was imaged with a high speed framing camera (HSFC) (model # 114, produced by Cordon). Test charges were positioned along the top edge of a grid board with 2.54 cm blocks and detonated using a split fire pulse to initiate the camera. Examples of the images produced are provided in Figure 2 where the imaging duration was 5 µs per-frame for 25 frames on color slide film. These images provided particle front formation, velocity information and identification of early time combustion for the first 125 µs.

Measurements particle front were determined from HSFC imagery. The distance from the surface position to the leading edge of the particle front was done at discrete time intervals from a position within the middle 25 percent of the charge. Adjustments to this position were done to account for instabilities in the particle front resulting from jetting or particle flow not perpendicular to the charge surface. Measurement positions once set within the 25 percent region were not adjusted to ensure that the proper flow progression was repeatedly measured. Measurement error included the maximum variation from instabilities in the particle front, and any variation in the boundary between the particle front and air resulting from inadequate lighting or focusing.

To ensure reproducible test results, control of the charge configuration and powder volume was maintained within each series. Additionally, multiple test firings of each configuration were performed for statistical validity. The charge volume was controlled by having the internal diameter of the paper tube built to 1.00±0.006 inch which maintained an annular space of 6.35 mm between the explosive core and the tube wall. X-ray images were made of all the test charges to ensure no defects such as air pockets in the powder or misalignment of the glued explosive pellets were incorporated into the test charges.

For the PIV imaging, each test charge was hung 218.4 cm from the chamber floor. The position was recorded with a digital photograph from a small hand held camera and a video image of the field of view (FOV) location was made using the PIV camera against a 1 cm marked grid backdrop. The light sheet thickness for all PIV shots were checked prior to each test via burn paper and were measured to be 1.6 mm at the center of the camera FOV. A set of setup images were recorded each time before the start of every test with the test charge number recorded in both the setup image and PIV software.

A 7.5-volt transistor-transistor logic (TTL) signal from the fire control hardware was split and sent to both the PIV system software and the charge detonator. A difference in cable lengths accounted for only about a 30 ns difference in pulse arrival times (3 ns/m) between computer software and the detonator in the explosive train.

2.1. Numerical Simulation

Model simulations were conducted on the metal powders and solid shell test item configurations. As described by Tanguay et al. (2007), body forces such as gravity on a particle in the detonation products is only subject to a drag force. Therefore, the one dimensional model used in the simulation is governed by Newton's second law:

$$m\frac{dv_p}{dt} = \frac{1}{2}C_D A_{cs}\rho_t |u_t - v_p|(u_t - v_p)$$

(1)

where m is the mass of the particle, A_{cs} is the projected area of the particle, C_D is the total drag coefficient, ρ_t is the density of the fluid, u_t and v_p are the fluid and particle velocities.

The Klyachko drag equation (Fuchs, 1964) was used to estimate the drag coefficient (C_D) for the H-95, H-10 and W-27 particles at 1 m from the charge using the particle velocity results from the HSFC and PIV imagery. The mean diameter values of the H-10, H-95 and W-27 where used in the calculation assuming the PSD did not change from the starting material. The result is a single averaged approximation for the drag coefficient at one meter. Drag coefficients (C_D) values were calculated using Klyachko's drag equation (Fuchs 1964) is represented as:

$$C_D = \frac{24}{Re}\left(1 + \frac{(Re)^{2/3}}{6}\right)$$

(2)

where *Re* is the Reynolds number assuming an incompressible flow due to the relative insensitivity at low pressures of shear tensor in calculation of the Reynolds number. The Reynolds values were obtained using the Chinook hydrocode described in Dunbar *et al.* (2011). The drag model is an incompressible correlation for Reynolds numbers less than 1000 (Saito *et al.* 2003). Gas sound speed was initially fixed in the Mach number with an estimated molecular viscosity in the Reynolds number. With adjustments to the sound speed, recalculation of the model estimated low relative velocity, low Mach numbers, and low Reynolds numbers. This indicates that the drag model used was appropriate to the flow regime.

Values for the numerical particle velocity and concentration at the FOV are provided with the Chinook code in a stepwise method (Chinook manual, 2006). Particles and fluid continua are modeled and tracked using an Eulerian solver during the initial detonation and dispersal period known as the profile step. Later at 9-10 μs, using the conversion solver, the particle masses are converted by the Lagrangian solver using the known PSD of the initial powder. During the next step, in the intermediate domain, particle groups are modeled and "mapped" into a larger domain allowing mesh resolution to be decreased. In the final full domain the resolution is again reduced to decrease mapping errors. This is the point at which the data for particle concentration was extracted.

Estimating particle concentration in PIV images can be labor intensive. A method identified by Stitou et al. (2006) in conjunction with the PIV software was used. A electronically generated grid with interrogation regions set at 64x64 pixels was over laid on to each particle field image. Each of the 64x64 interrogation regions were numbered and those with no particle images in the outer edge of the particle flow were masked out and not used in the concentration calculation to prevent skewing of the particle density. Several numbered regions were selected at random and the valid images counted in each region. The sum of the particle images within each region was then divided by the area of its region. All region values were then summed. The relationship for concentration is:

$$C_m = \sum_n^{i=1} \frac{N_{d_i}}{S_{w_i}} \tag{3}$$

where C_m is the particle concentration, S_w is the area of the interrogation region and N_d is the number of particles counted within the interrogation region.

Whether momentum transfer from a shock wave can result in an increase in particle velocity was evaluated using the equations identified by Zhang et al. (2003) for solid particle and gas shock interaction. The duration of time when the particle and shock are in contact is the shock interaction time, described as:

$$\tau = \frac{d_p}{D_0} \tag{4}$$

where d_p is the particle diameter and D_o is the shock velocity. For the response time of particles, the velocity relaxation term is:

$$\tau_v = \frac{4 d_p^2 \rho_t}{3 \mu C_D Re} \tag{5}$$

and μ is the fluid dynamic viscosity. The ratio of these two terms, the shock interaction time over the velocity relaxation time, provides a criterion to determine whether the shock will transfer sufficient energy to the particle to make a negligible change in increasing the particles velocity. Zhang et al. (2003) identified that typical numbers for even particles in the 0.1-1μm range for the shock interaction to the relaxation time was three to four orders of magnitude smaller, therefore, the particle would have negligible changes in its velocity as it crosses the shock front.

3. RESULTS

The most profound differences in the particle patterns and velocities were observed between the different charge series. Early expansion pattern differences at 50 μs can be seen of the powdered aluminum in Figure 2a,b compared to the tungsten powder in Figure 2c and solid aluminum shell baseline in Figure 2d. Frame data from the HSFC images showed different particle front expansion rates with the smaller aluminum particles being the quickest accelerated and the tungsten powder (W-27) being the slowest. A listing of charge configurations, mean

5

experimental velocities and numerically estimated velocities using the Chinook model are provided in Table 2. The images also clearly show greater luminescence with the H-10 which has a larger quantity of smaller particles. These observations are in good agreement with Frost *et al.* (2002) in which magnesium spherical particles in a spherical or cylindrical charge case was used with sensitized nitromethane. Frost *et al.* (2002), determined that for a given charge diameter, if the charge size is large enough and ignition occurs, the smaller the particle size the more prompt the ignition and the greater the luminosity. For comparison purposes, the high melting point of tungsten at 3422C provides a stark contrast to the reactive soft aluminum material which has a melting point of 660C. The PIV particle images were clear and sharp with luminescence blocking the center most portion of some particle fields. With tungsten, there was an absence of luminescence from burning particles and gas, particle structure formation; a relatively well distributed particle field with little or no agglomerated particles was also identified.

The average mass of the aluminum solid shells were 4.5% less than the H-10, and 19.0% less than the H-95 powder charges. The mass differences in the powder charges were due to the differences in the PSDs and the resulting packing densities. The tungsten charge was as much as 8.8 times greater in mass than the aluminum solid shell case charge due to its greater material density of 19.3 g/cc and packing density from the wide PSD verses aluminum's 2.7 g/cc and narrower PSD. The wider PSD allows for small particles to fit between the larger ones, resulting in a greater mass per charge for the same material types.

4. ANALYSIS

4.1. Image Processing

No post processing of the PIV images to reduce luminescence was required to improve the total number of good image pairs for the tungsten powder charges. Background subtraction for the aluminum powder charges were needed to enhance the particle images due to luminescence. This procedure eliminated some of the false images in the deep field and reduced the low intensity ghost images from particle outside of the light sheet. The image enhancement process entailed an estimate of background luminosity from each frame, the value was then subtracted from the entire image to proportionally reduce the luminosity across the image. Images were processed separately with their own background estimate. The use of advanced PIV image processing was necessary during vector processing of the aluminum powders and the solid aluminum shell charge fragments to track non spherical images. For the aluminum powders, though most retained their spherical shape, many did not and the formations of agglomerates and larger structures added complexity to the particle field.

The most effective grid engine processor used in this study proved to be a combined use of image deformation and image normalization with the Hart correlation approach. This combination provided the maximum number of good vectors through greater measurement accuracy in complex flows. The Gaussian mask was used for the spot mask engine and Gaussian peak engine while using square interrogation regions for image correlation. Post-processing used a global and local validation processor and vector field conditioning setup when recursive hole filling was needed. Mean particle velocity sensitivity with and without recursive hole

filling values were compared on all velocity analysis and was shown in most cases to not differ more than 5 percent. The use of a processing mask reduced the effect of smoothing the mean velocity value by reducing the number of interpolated vectors for those cases where recursive hole filling was needed. A universal median test was used for local validation to remove bad vectors it is an improved median filter which is a more robust validation method than the mean because it is less sensitive to the flow field. Vector field conditioning used the local median for filling holes in the interrogation regions which failed validation.

The vector analysis settings differed slightly from each image set and from each powder series in order to maximize the percentage of good vectors. Lost images fell in three categories: 1) particle images lost from in and out of plane motion within the FOV 2) images which were lost from high background luminosity; or; 3) those lost within dense image structures where the individual particle images or a significant portion of their edges could not be determined. These types of losses are common in blast wave imaging due to the sudden acceleration and heating, material type, and projected solid angle influence of the curved surface at increasing radial distances.

4.2. Particle Velocity and Concentration

For H-10, the particle number was not able to be determined because of the large amount of clumping and overlapping of the individual particle images. For the H-95 experimental data, the average number of valid images in the FOV was determined to be 9.4×10^5 giving 12 particles per mm^3 in the FOV for W-27, the average number of particles was 9.7×10^5 or 12 particles per mm^3 in the FOV. In contrast the simulation generated the average number of particles in the FOV to be 706 (9 particles per 1000 mm^3), 9.10×10^5 (11 particles per mm^3), 2.85×10^4 (4 particles per 10 mm^3) for H-95, H-10 and W-27 respectively.

For the solid shell, 1,948 particles were tracked experimentally by the PIV in the FOV, but only three were tracked in the simulation. Two important differences in the solid aluminum shell experimental and simulation comparison are the arrival times at 1 m and the particle breakup model. The numerical image at 0.95ms showed three particles within the FOV with a average velocity of 668 m/s. This is a 23 percent greater velocity than the PIV value. The difference in the time interval values between the experimental and numerical model can be explained from the breakup and drag model used by the simulation. The simulation model for this research used an Eulerian solver to simulate the initial expansion of the metal case in a fluid phase, this fluid is later converted to fragments after reaching a specified failure strain. At this point the fragments dispersal is simulated using the Lagrangian solver. Application of the Klyachko drag equation numerical model is based on a spherical metal fragment distribution with a 1 mm mean diameter, this provided a representation that is significantly different from the experimental condition with large irregular fragments. The simulation used this method because the PSD of the fragments were not known and could therefore not be applied to the dispersion model. Calculations from the HSFC indicate the fragment arrival time to be 0.848 ms compared to the simulation time of 0.533 ms. This relates to an experimental particle velocity of 1.5 km/s and a numerical predicted velocity of 1.8 m/s or a 300 m/s difference in velocity, hence different arrival times at 1 m

Distribution A, Approved for Public Release: 96ABW-2011-0255

A complete distribution was not recovered and for those fragments that were recovered many had large aspect ratios with dimensions of as much as 30 mm long by 4 mm wide. Clearly these fragments deviated from the small spherical particle conditions imposed on the PSD for the simulation in both mass and shape resulting in significant error between the experimental and numerical values. From Equation 1, differences in the experimental particle drag due to the irregular shape and increased area of the fragments becomes the dominate force for a later experimental arrival time at the FOV. For all of the powder charges the PSD was known and was utilized in the simulation models. Results from the numerical model compared favorably with the powder experimental values listed in Table 2.

4.3. Early Time Powder Front Velocities

A comparison of the particle front velocity for the aluminum and tungsten powders at early time showed a significant difference among the different charges. The H-10 aluminum powder has good linearity after 50 µs seen in Figure 4 from its quick acceleration by the fluid. The plots show that as the particle mean PSD increases, the particle front velocity decreases and later becomes nearly constant after its initial acceleration period. This is in agreement with predictions from Engelhardt (2006) simulation, Cooper (1997), Frost et al. (2005) and Dunbar *et al.* (2011) for spherical metallic particles of different sizes.

After its initial acceleration, W-27 begins to slowly decrease in velocity and at 1 m it is at a higher velocity than any of the aluminum powders (Table 2). Tungsten powder is about seven times the density of aluminum, thus it provides additional confinement with a greater transfer of energy to the particle shell. The smaller and less dense particles of aluminum accelerate faster and approach equilibrium quickly with the high velocity product gas behind the shock; hence, they achieve a higher dispersal velocity. Some very small low density powders like H-10 have a large quantity of very small powder sizes below the mean which can be quickly accelerated by the initial shock and product gases. This event can be seen in the PIV image of Figure 4, set at 35.6 cm from the charge surface.

The aluminum solid shell fragments continue to accelerate beyond the time period shown because of their greater mass and stored energy. Their higher stored energy comes from the greater pressure volume (PV) work of the product gases due to the added confinement of the shell prior to breakup. Because of the greater fragment masses, the inertia effects require a longer acceleration period to attain their maximum velocity and a longer deceleration at 1.0 m means higher velocities at the FOV.

Fragments from the solid shells were modeled with a projected area of a rectangle for estimating the drag coefficient. Many of the fragments had large length to width ratios and were imaged in early time shortly after case breakup. The size distribution that is imaged is contrary to the simulation model which is described as a normal distribution with a mean particle size of one millimeter. This was later shown to affect the differences between the experimental and numerical arrival times, velocities and number concentration at the FOV.

Error measurement grew with increasing time for each system tested. Instabilities increase as the powders expands; for the solid particles the size, shape and ordination vary

8

enough to significantly change their leading edge from frame to frame due to the particles rotational velocity. This causes the solid particle to blurs and makes it difficult to identify a defined edge.

4.4. Particle, Fireball and Shock Interaction

As has been seen in the PIV images for all of the aluminum powder systems (Figures 10b, 11b), structures of agglomerated particles existed within the blast wave. These structures vary somewhat in character depending on several factors including the initial PSD, total mass of the particle bed, the bed packing density and thickness. The agglomerations in the structures are a combination of induced agglomeration due to shock at early time and particle heating and burning from the intrusion of product gases into the particle bed. Particle fragments were also identified in the imagery indicating that particles underwent severe plastic deformation and failure as reported by researchers using numerical simulations (Tanguay *et al.* 2007).

The greatest opportunity for particle, fireball and shock interaction occurs at early time (0-10µs) with the primary shock and intrusion of hot product gases occur within the particle bed prior to the cardboard shell splitting. Velocity and temperature transmission factors described by Ripley (2007) and momentum transfer to solid particles by Milne (2000) and Zhang *et al.* (2003) provide the mechanism for agglomeration at early time. Simulations describing particle and shock position in early and later time for each of the powder series are provided in Figures 5-7.

For H-10 the first early time crossover of the shock wave and particle field occurred at 0.09 ms and 0.18 m (Figure 5a). Calculations of the ratio of the shock interaction time to the velocity relaxation time gave a value of 6.72E-4. The shock interaction time value is 3 orders of magnitude smaller than the velocity relaxation time. Thus from Zhang *et al.* (2003) the particle crosses the shock front with negligible changes in its velocity. Temperature of the air just behind the shock was determined from the Normal shock tables (Anderson 1997) to be 1740 K. The second H-10 shock interaction showed a smaller ratio also providing a negligible momentum transfer with the air temperature behind the shock of 834 K. In Figure 5b, it can be seen that the shock front velocity becomes linear which is representative of a sonic wave. Therefore, although the particle velocity did not significantly increase, energy would be transferred to the surrounding environment as heated air.

The H-95 had only one crossover point with the particle front and shock wave at 0.11 ms and 0.22 m (Figure 6a), with a shocked air temperature of 763 K. The shock interaction time to the velocity relaxation time ratio was 9.73E-5. The shock interaction time was 4 orders of magnitude smaller than the velocity relaxation time suggesting that the shock would not significantly affect the particle velocity (Zhang *et al.* 2003). The tungsten powder had no particle and shock crossing points due to its slow particle field velocity (Figure 7), thus no interaction was possible after the passage of the primary shock front from the H.E. reactive wave.

A comparison of all the powder series plots shows that shock and powder interactions available to form agglomerates took place during the initial particle shock up and expansion or before 0.15 ms. For H-10 the PIV image of Figure 4 was taken at 2.5 ms, with close inspection

9

this image shows signs that agglomerated structures have already formed and that some very small material is ahead of the main particle cloud. From the simulation plots of Figures 5-7, the 2.5 ms time is earlier than the second particle and shock crossover periods for H-10, implying that the second intersection of the two crossovers is not the primary event in forming the agglomerations. Additionally, the linear shock line in later time indicates a constant velocity which is consistent with a low energy acoustic wave incapable of containing enough energy to preheat the region between the shock and the particle front. For H-95, the particle front does not cross the shock front a second time within the 5.7 ms period. The first and only crossing point in Figure 6a occurs at 0.11 ms, and 0.22 m which is at a greater distance away from the charge surface than for the H-10 crossovers points. This provides for additional time for adiabatic cooling during the expansion period, reducing the temperature to 763 K. In addition, for the H-10 powder, the simulations show first crossovers of the shock and powder fronts between 80 and 100 µs, earlier than for H-95 and less opportunity for cooling. During the period between 20-120 µs, the HSFC powder images showed developing combustion in the particle front which would provide an opportunity for the hot particles to be forced together and agglomerate.

The zone just behind the shock at the first cross over point is at a higher temperature than the fireball because it is shock compressed. This zone also has a higher oxygen concentration than ambient and provides an additional opportunity for particle heating and burning, thereby, promoting additional agglomeration. Images in Figure 2 at 50 µs show a lessening of combustion as particle size increases. A decrease in aluminum particle combustion as the diameter increases has also been reported by Zhang, (2005) for aluminum and Frost *et al.* (2005) for magnesium particles.

The W-27 in contrast to the reactive aluminum with its high melting point and greater hardness produced no agglomeration or particle structure formation seen at one meter. Its high density resulted in slow acceleration with high inertial properties leading to a higher velocity than the other powder charges in the PIV FOV. Simulation results revealed an average drag coefficient for the W-27 powder that is lower than for the aluminum powders at 5.7 ms with a measured experimental velocity of 50.5 m/s.

4.5. Particle Velocity Gradient within the Particle Field

From twelve PIV H-95 charges, velocity analysis was conducted on three horizontal band regions within each imaged particle field. The bands were positioned at the same location in the FOV for every one of the twelve frame pairs. This provided velocity data at distinct locations within the FOV, enabling a mean velocity and standard deviation for each band to be determined. Figure 8a is a representation of the approximate location of the three velocity band regions. From Figure 8b it can be seen that the mean particle velocity is slowest at the top of the FOV in Band 1 and fastest at the bottom of the FOV in Band 3. In Band 2 the mean velocity was lower than for Band 1 or Band 3. The standard deviation was greater in Band 2 than for Band 1 or Band 3, indicating that the range of velocities were greater than in the other bands. In Band 2 a higher percentages of negative velocities were measured by the PIV analysis software indicating directional changes and turbulent mixing.

Distribution A, Approved for Public Release: 96ABW-2011-0255

4.6. Experimental Reproducibility

Considerable importance was placed on the ability to demonstrate repeatability of the measured velocity values from the particle fields generated by the test charges. Twelve H-95 powder and six H-10 charges were produced, screened and tested under identical conditions and placed at the same relative position as described previously. After processing the images and generating a velocity contour plot of the shot, the mean velocity values were imported into a statistical process control software package (Petrovich, 2007).

Figure 9a for H-95 and Figure 9b for H-10 show that the velocity means of each experiment falls within two standard deviations of the mean value. For the determination of the vector distribution normality, the combined 42,228 vectors from the twelve H-95 shots were used. A normal distribution with a mean of 7.75 m/s and a standard deviation of 0.84 m/s was calculated. A vector count of 7,563 from six of the H-10 shots were also determined to have a normal plot, with a mean of 5.79 m/s and a standard deviation of 1.38 m/s. Both data sets passed the normality tests in the statistical package using the Anderson-Darling, Shapiro-Wilk and Lin-Mudholkaria criteria for a normal distribution of velocities. Both charts indicate a random fluctuation about the mean. This meets the standard criteria for an in control process which can be repeated.

Although the H-10 series did not have the 12 independent shots like H-95, through similarity of construction and testing the H-10 measurements can be shown to be in control and can be qualified as a repeatable process. The calculated mean particle velocity for each PIV event includes the measurements of all valid particle images. The mean particle velocity having been derived from thousands of Individual particle measurements thus has a solid statistical basis. Figures 10-13 provide views of the FOV from the numeric model and HSFC, and PIV imagery for the three powder types and the solid aluminum shell.

5. CONCLUSIONS

This research demonstrated success in imaging and determining velocity values of small metallic particles driven by the product gases of an explosive using an HSFC and PIV. Imaging the different particle materials showed a stark difference in characteristics between aluminum powders of different sizes and a tungsten powder. Due to shock compression, heating, and aerodynamic attraction, large and dense particle structures were produced by the aluminum powders. Tungsten powder, in contrast, was well distributed with little or no agglomeration and showed little luminosity with individual particles being generally less bright than aluminum particles. The images clearly show that changes in material type and the particle size can significantly affect the speed, agglomeration of particles and the particle structures within the flow field. The study also demonstrated the ability to use the PIV imagery for determining a particle velocity gradient within a flow field. The velocity gradient provides an explanation for the lengthening of the particle field at increasing distances. This phenomenon provides a natural separation method of the particles with the larger particles leading the particle field. Additionally, an effective method to determine the drag coefficients for the different particle fields using two experimentally determined velocity values was demonstrated with results comparing well with the numerical model results. This provided confidence that the model has

11

the ability to provide usable comparative data. Because the drag model estimated low relative velocity between particles and fluid, low Mach numbers, and low Reynolds numbers with experimental velocities comparing well at the FOV, it can then be inferred that the drag model was appropriate for the flow regimes reviewed.

Trends in the simulations using a fine mesh resolution to accurately capture the shock and particle dispersal provided numerical results which identifies the H-10 particle front overtaking the shock front earlier than the larger H-95 particles due to a higher overall drag force. For H-10 it was shown that the shock particle interaction time is short and the velocity interaction time is very long, producing a very small ratio. This indicates that the primary acceleration of the particles are due to viscous drag immediately behind the shock front, and not shock acceleration; this is consistent with Zhang *et al.* (2002) results. The simulation also showed that the tungsten behaves more like H-95 than a small diameter powder and at later times its velocity is greater at 1 m because of its greater mass induced inertia.

The combined imaging capability of HSFC and PIV can provided a practical method to aid in the validation of detailed model algorithms designed to investigate mixing, particle burn phenomena and particle concentration for hydrodynamic codes such as Chinook and the CFD code Second-Order Hydrodynamic Automatic Mesh Refinement Code (SHAMRC). The accurate characterization of these phenomena is a significant effort and of high priority for complex blast models.

ACKNOWLEDGEMENTS

REFERENCES

Anderson, J.D. (1997). Fundamentals of Aerodynamics. (4th ed.). McGraw-Hill. ISBN 0071254080.

Balakumar, B.J. and Adrian, R.J. Particle image velocimetry in the exhaust of small solid rocket motors. *Exp. in Fluids* **36**, 166-175, 2004.

Chinook keyword input manual, Software manual #SM-07-06, Rev.27, Martec Limited, 1888 Brunswick Street, Ste 400, Halifax, Nova Scotia B3J3J8, Canada, 26 Apr., 2006.

Cooper, P.W, Explosive engineering. Wiley & Sons, New York, NY, 1997.

Dunbar, T., Ripley, R.C., Donahue, L., Numerical simulation of particle dispersal from explosives surrounded in a layer of metal. Martec Technical Report TR-10-27, Aug. 2011.

Donahue, L., Ripley, R.C., Horie, Y., Jenkins, C.M., & Zhang, F. Cylindrical explosive dispersal of metal particles. APS15, 2007.

Engelhardt, Christopher, M. Numerical modeling of heterogeneous high explosives, AIAA - 40th thermophysics conference, 6(2008).

Frost, D.L., Goroshin, S., Levine, J., Ripley, R., Zhang, F. Critical conditions for ignition of aluminum particles in cylindrical explosive charges, *14th APS Conference on Shock Compression of Condensed Matter,* Baltimore, Maryland, 2005.

Frost, D.L., Ornthanalai, C., Zarei, Z., Tanguay, V., and Zhang, F. Particle momentum effects from the detonation of heterogeneous explosives. *J. of Applied Phys.***101**, 113529, (2007).

Frost, D.L. and Zhang, F. The nature of heterogeneous blast explosives. Proceedings of the 19th International Symposium on the Military Aspects of Blast and Shock. Calgary, AB, Canada, 2006

Frost, D.L., Zhang, F. and McCahan, S. Critical conditions for ignition of metal particles in a condensed explosive. 12th. Int. Detonation Symposium. San Diego, Ca, (2002).

Fuchs, N.A.(1964). The mechanics of aerosols. Macmillan Co., New York. N.Y.

Gagliardi, F.J., Chambers, T.D.,Tran, Tri-D. Small-scale performance testing for studying new explosives. 6th VACETS Technical International Conference, UCRL-CONF-212196, Milpitas, Ca, USA, June 4, 2005.

Jenkins, C. M., Horie, Y., Wu, C-Y. Particle velocity and structures in blast waves imaged using particle image velocimetry, *Int. J. of Multiphase Flow,* 36, p88-91, 2010.

Milne, A.M. Detonations in heterogeneous mixtures of liquids and particles, *Shock Waves, 10*, 351, 2000.

Murphy, M.J., Adrian, R.J., Stewart, S.D., Elliott, G.S., Thomas, K.A. and Kennedy, J.E. Visualization of blast waves created by exploding bridge wires. *J. of Visualization* **8**, 125-135, 2005.

Petrovich, M. V. MVPstats: MVP Programs, ver. 20071215, (2007).

Ripley, R.C., Zhang, F., Lien, Fue-Sang. Acceleration and heating of metal particles in condensed explosive detonation, CP955, APS *Conference on Shock Compression of Condensed Matter*, Baltimore, MD, edited by M, Furnish, M. Elert, T. Russell, and C. White, American Institute of Physics, Melville, NY, 2007.

Saito, T., Marumoto, K. and Takayama, K. Numerical investigations of shock waves in gas-particle mixtures. *Shock Waves,***13**, p299-322, 2003.

Stitou, A. & Riethmuller, M.L. Progress in PIV-PTV methods: application to concentration measurements, 11th International Symposium on Application of Laser Techniques to Fluid Mechanics, Lisbon, Portugal, July 8-11, 2002 VKI RP 2002-36.

Tanguay, V., Higgins, A.J. and Zhang, F. A simple analytical model for reactive particle ignition in explosives. *Prop. , Explosives, Pyrotechnics* **32**, No. 5, 2007.

Zhang, F., Frost, D.L., Thibault, P.A., and Murray, S.B. Explosive dispersal of solid particles. *Shock Waves* **10**, 431-443, 2001.

Zhang, F., Thibault, P.A. and Link, R. Shock interaction with solid particles in condensed matter and related momentum transfer, Proc. R. Soc. Lond. A., **459**, 705-726, 2003.

Zhang, F., Yoshinaka, A., Frost, D., Ripley R.C., Kim, K., Wilson W. *13th Int. Det. Sym.* Norfolk, USA., 2006.

Table 1. Charge Mass Properties

Charge Type	Average Annular Powder Mass (g)	Average Tap Density (g/cc)	Average Total Charge Mass (g)
Aluminum Powder (2.70 g/cc)			
H-10	23.10	1.60	53.98
H-95	26.30	1.82	56.65
Thick solid shell (3.2 mm)	22.1	na	32.60
Tungsten Powder (19.3 g/cc)			
W-27	215.80	14.9	241.80

Table 2. Measured HSFC and PIV Velocity Values and Numerical Values

Charge Type	Exp. Early Time Velocity (Km/s)	Numerical Velocity (Km/s)	Exp. PIV Velocity(m/s)	Numerical Velocity (m/s)
Aluminum				
H-10	1.53	1.75	5.79	6.10
H-95	1.32	1.78	7.75	16.6
Solid Al shell	1.69	1.90	512.0	668.0
Tungsten				
W-27	1.29	0.80	50.5	55.3

Table 3. Experimental and Simulation Derived Drag Coefficients with Shock Velocity Interaction Time Ratio

Charge Type	Experimental Average Drag Coefficient	Simulation Average Instantaneous Drag Coefficient	Ratio of shock Interaction Time to Velocity Interaction time at crossover points $\left(\dfrac{\tau}{\tau_v}\right)$
Aluminum			
H-10	0.36	1.08*, 6.97**	6.72E-4
H-95	1.93	0.86*, 8.25**	9.73E-5
Solid Al Shell	0.36	NA	NA
Tungsten			
W-27	2.46	0.87*, 6.51**	NA

* Values are determined at 1.0 meter

15

** Values are determined at 0.44 meter
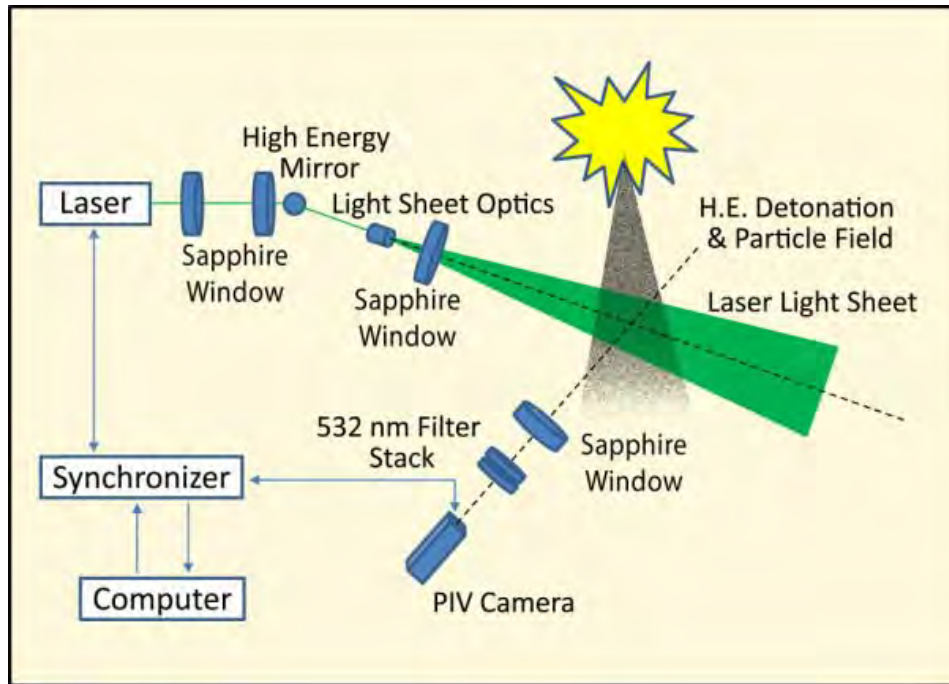
Figure 1. PIV test setup (view top down), high explosive was set above the light sheet with particle flow in a downward direction.
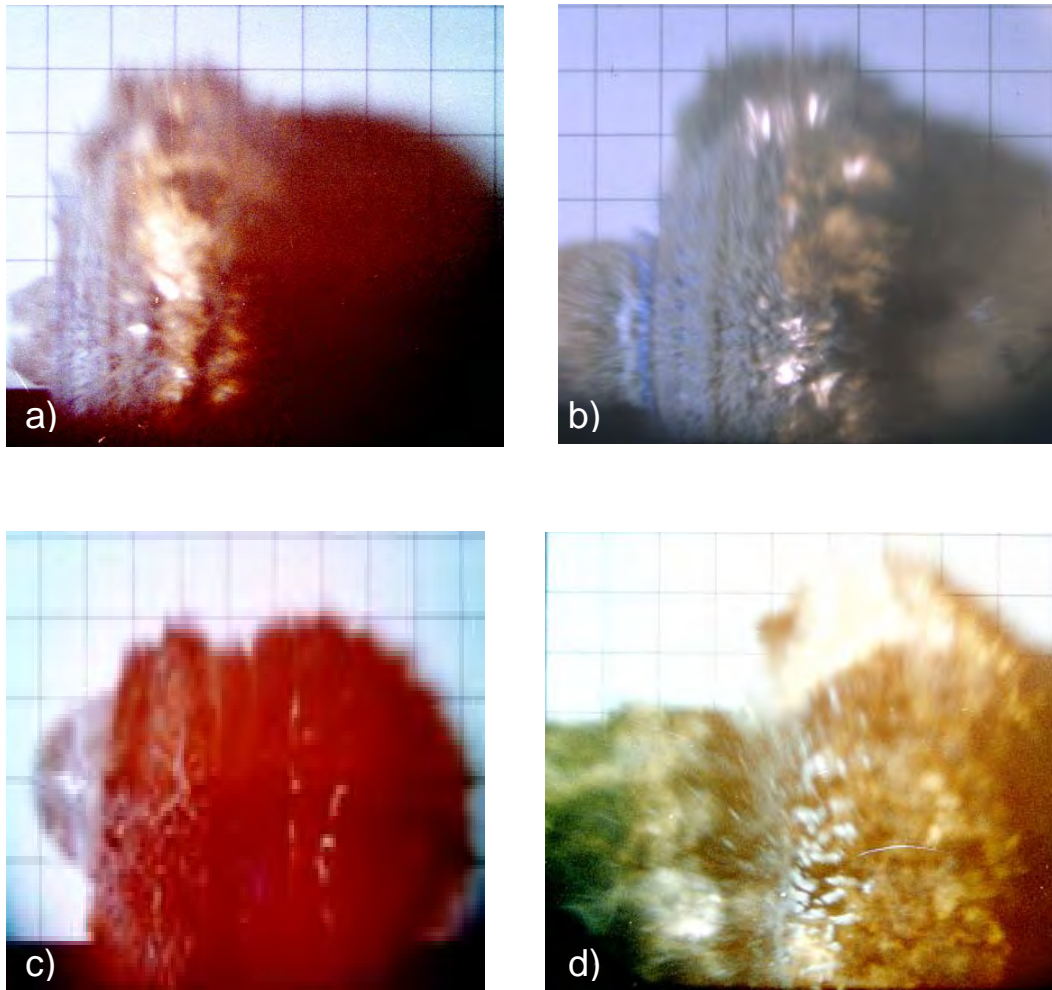
Figure 2. Early time expansion (a) An H-10 powder annulus charge at 50µs after initiation from the right side, (one inch per block) (b). 95 powder annulus charge at 50µs after initiation from the right (c) tungsten particle charge at 50µs into expansion, no combustion due to the inert metal powder (d) HSFC speed images of TSS case breakup with fragment images at 50 µs post detonation
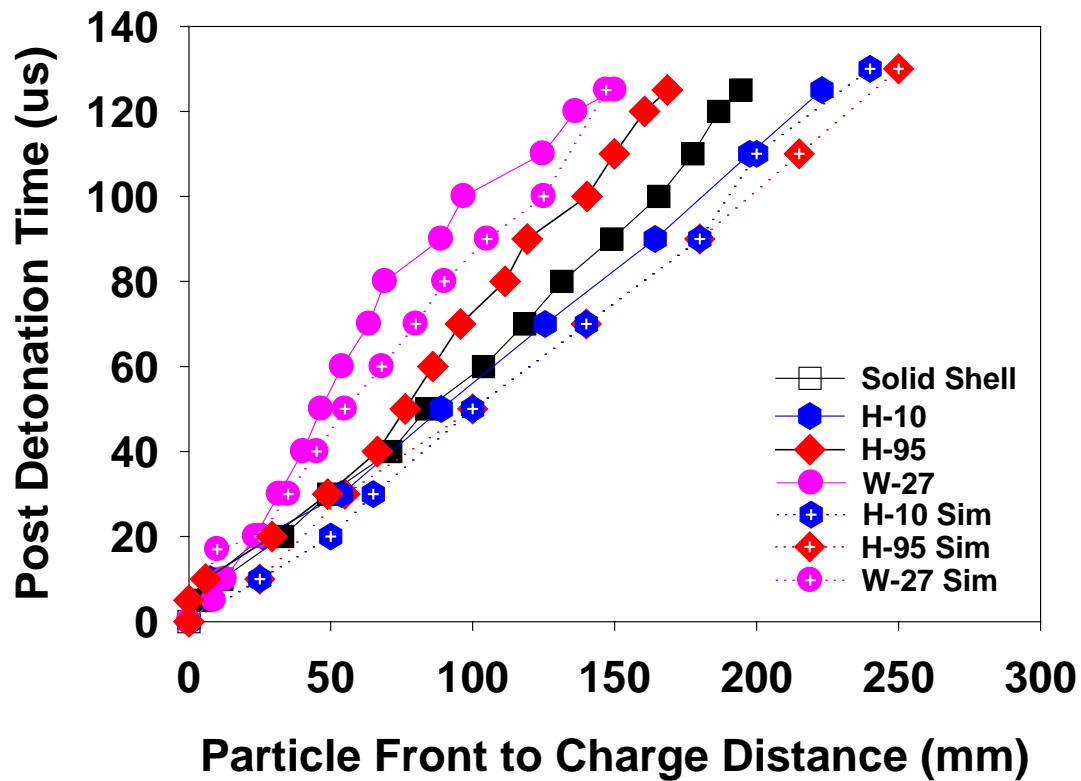
Figure 3. Early time experimental and numerical expansion data. The H-10 powder is linear after a quick acceleration in the first 30 μs. W-27 can clearly be seen lagging in the early acceleration and slowly continuing past 125 μs. Error bars are smaller than data point figures.
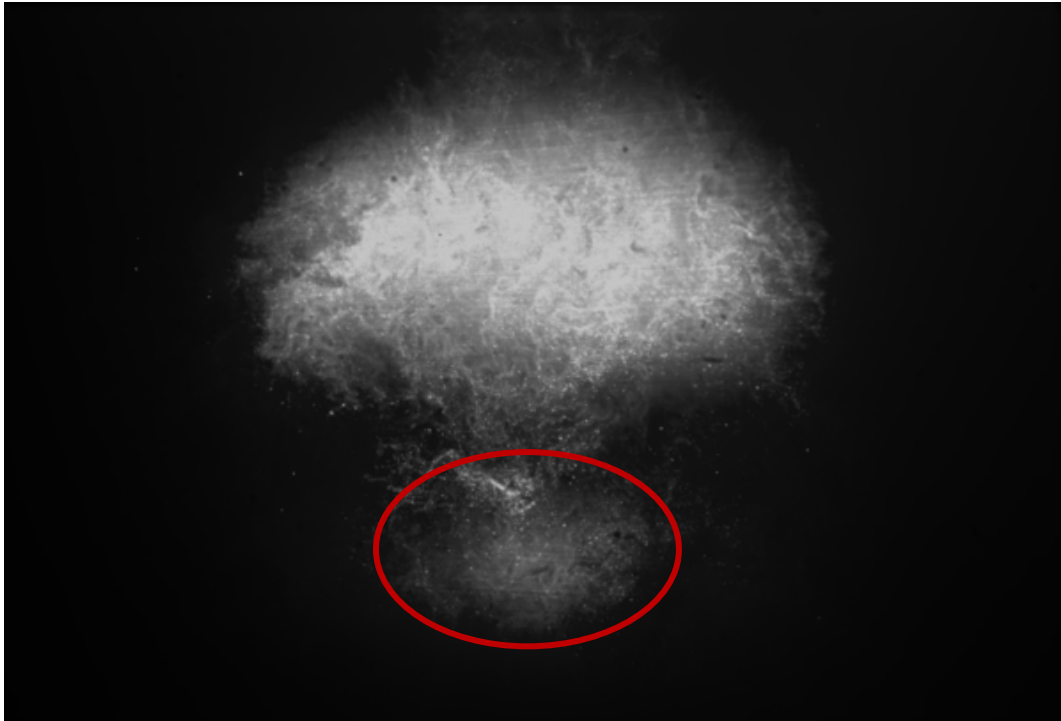
Figure 4. H-10 particle fields moving from top to bottom, at 44.7 cm from charge surface, 2.5 ms post detonation. A small particle cloud (in red) ahead of the main particle body may be due to acceleration of very small particles to near gas velocity. Upon close inspection some threads or regions of high particle content can be seen to be forming within the cloud.

a)

a)
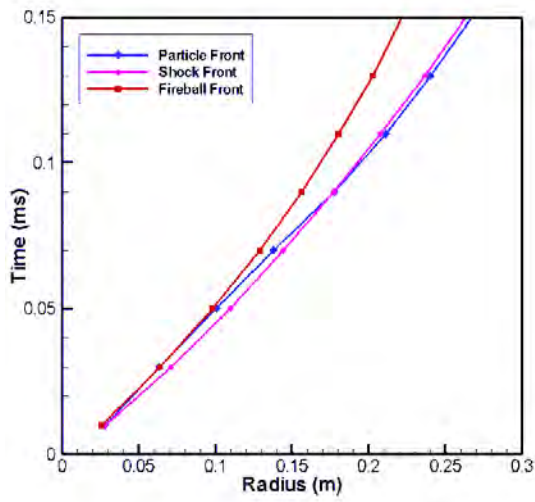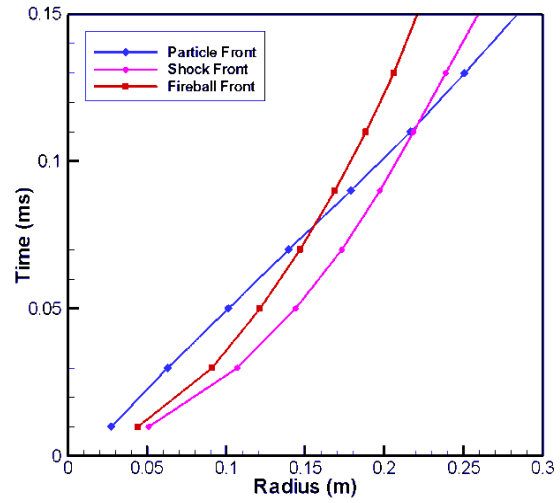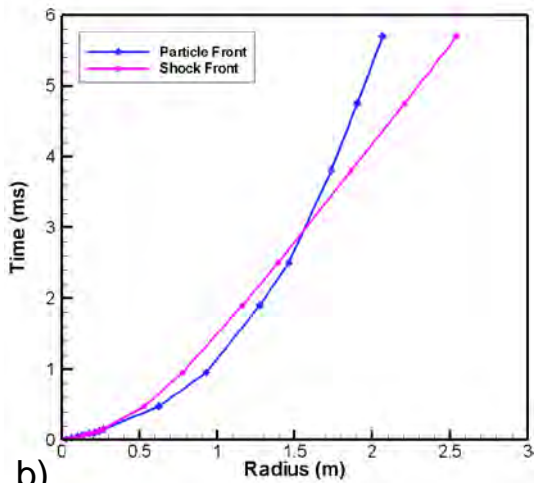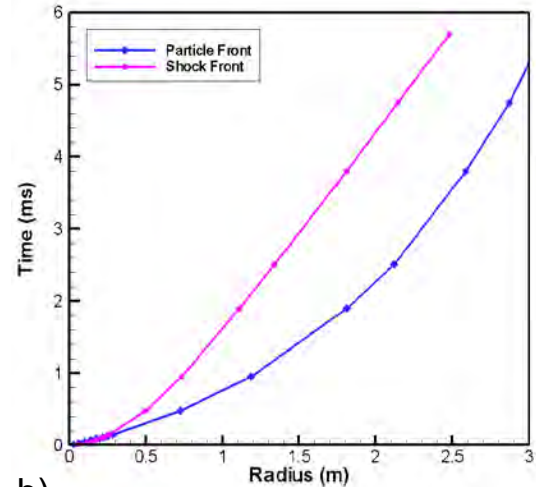
b)

Figure 5. Particle and shock front trajectory for the HMX explosive surrounded by 23.1 g of H10, (a) t = 0 – 0.15 ms. (b) full simulation t = 0 – 2.5 ms (Dunbar *et al*. 2010).

b)

Figure 6. Particle and shock front trajectory for the HMX explosive surrounded by 26.3 g of H-95, 0-0.15ms, (b) full simulation t = 0 – 2.5 ms (Dunbar *et al*. 2010).

20
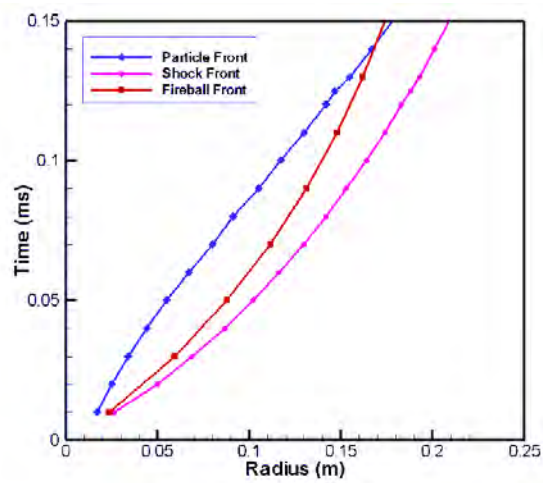
a)
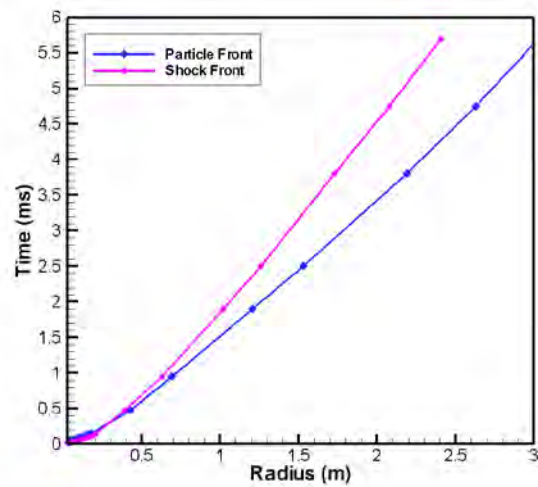
b)

Figure 7. Particle and shock front trajectory for charge with 215.8 g of W-27 (0 – 0.20ms) (Dunbar *et al*. 2010)

21
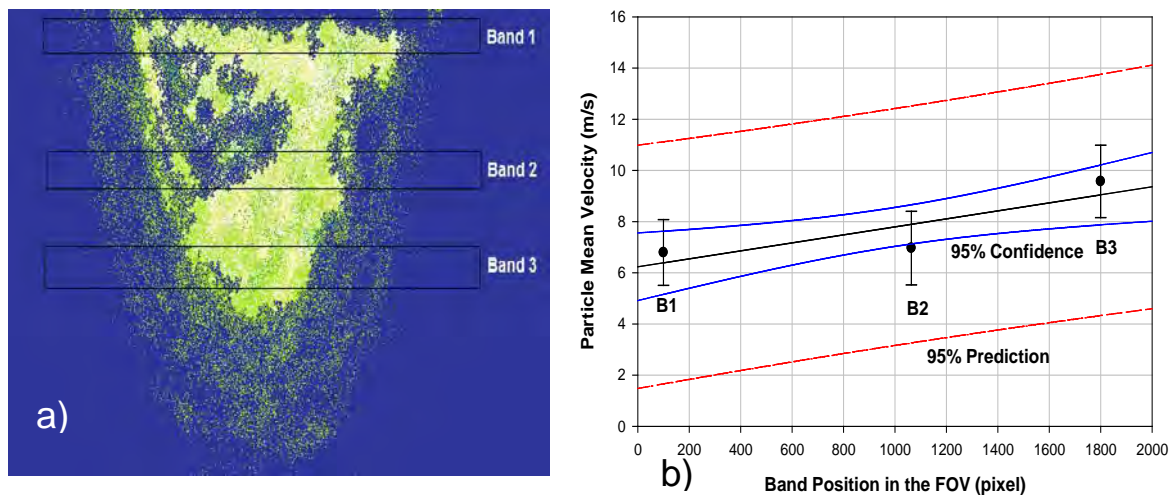
Figure 8. Representation of a PIV image (a) band zones displayed from which a particle velocity gradient was established (b) Particle band mean velocity values from the H-95 powder series.

Distribution A, Approved for Public Release: 96ABW-2011-0255
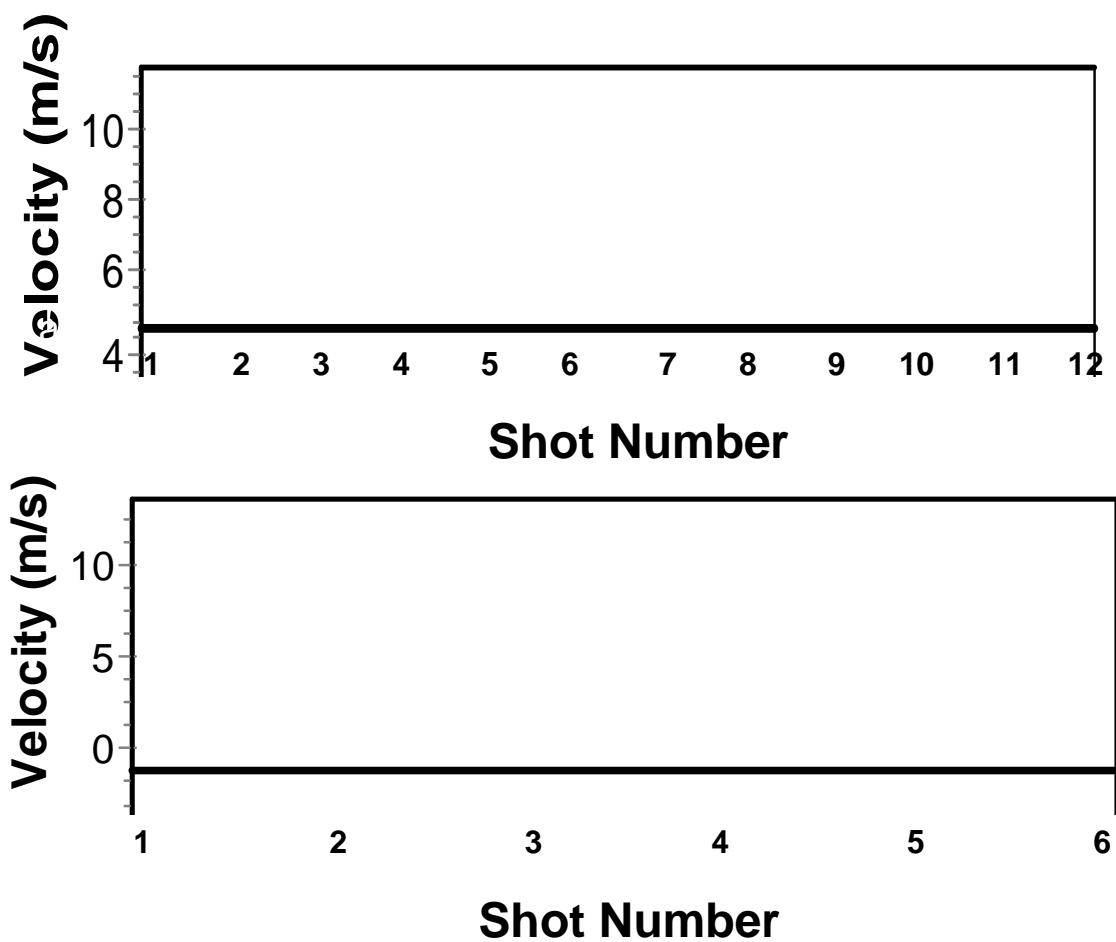
Figure 9. Mean velocity vs shot number (a) As measured H-95 experimental mean particle velocities of the image pair for each of 12 test shots. Mean velocity of all shots is 7.75±0.84 m/s within the FOV. (b) As measured H-10 experimental mean particle velocities of each image pair for vectors calculated within the FOV. Mean velocity of all shots is 5.79 ± 1.38 m/s within the FOV.

23
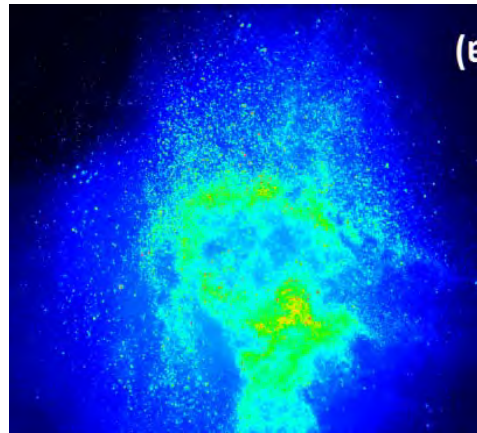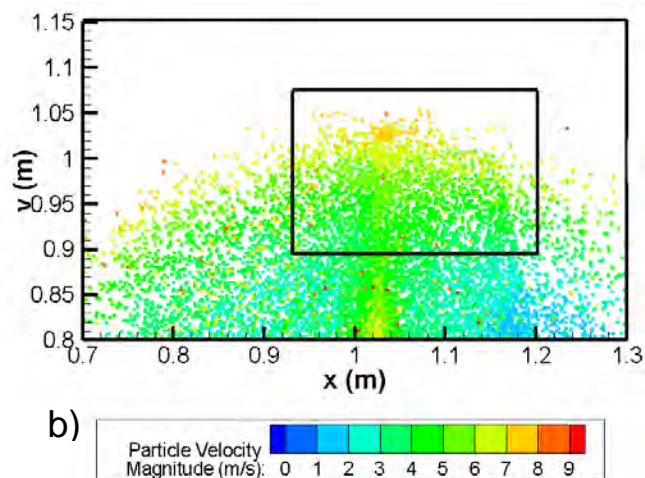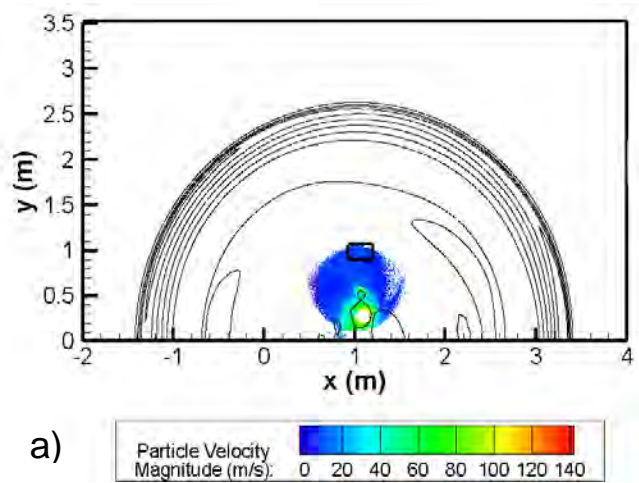
Figure 10. (a) Particle dispersal simulation for HMX charge surrounded by 23.1 g of H-10; right, visual image from HSFC, estimated position of PIV image within red box (b) Close-up of particle tracking window in (skip every 5th particle group), with a numerical mean velocity of 5.50 m/s right, raw PIV image cropped to remove empty image space.
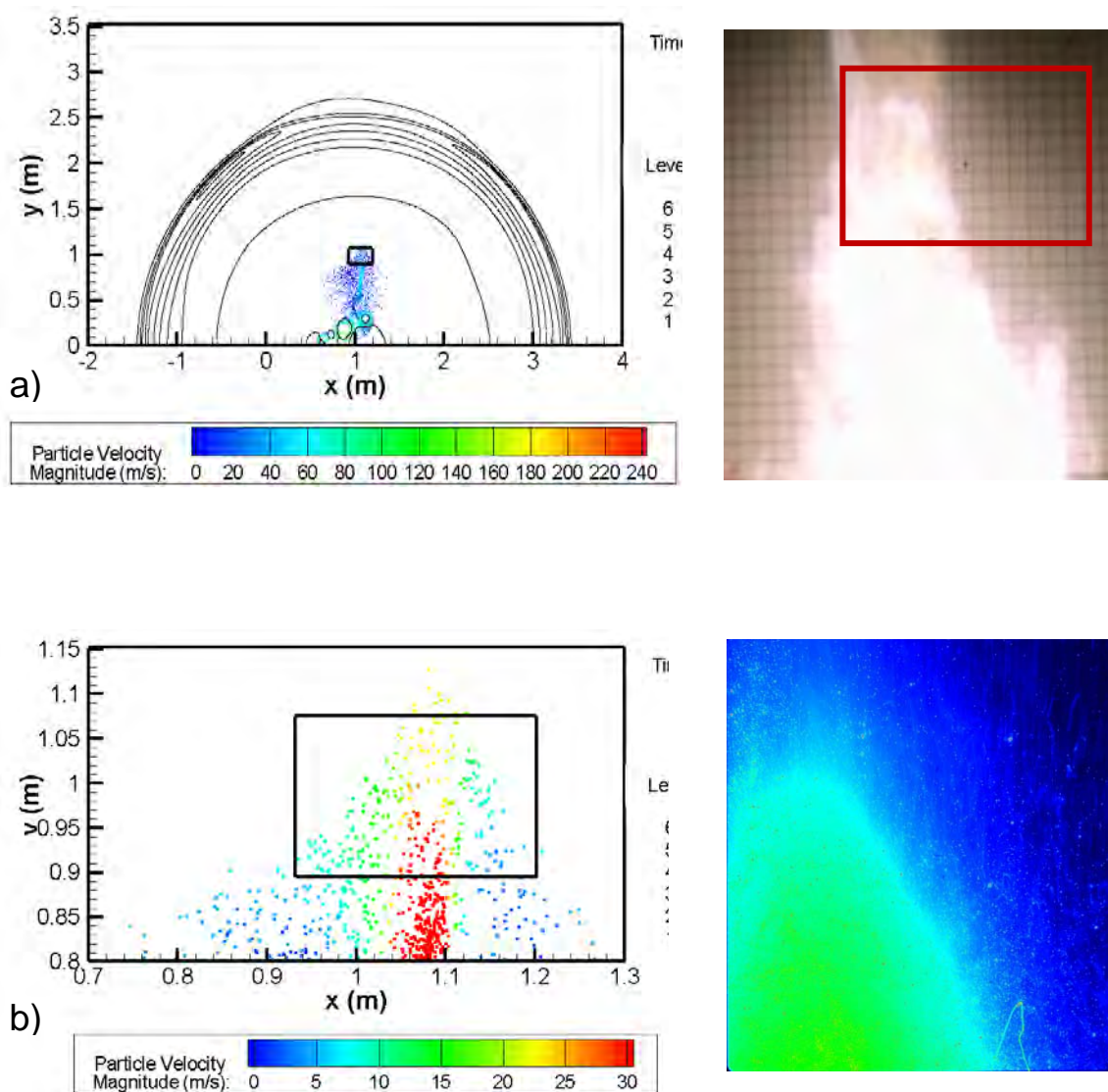
Figure 11. (a) Particle dispersal simulation for HMX charge with 29.8 g of H-95; right, visual image from HSFC, estimated position of PIV image within red box (b) Close-up of particle tracking window (assuming small particle counts cannot be visualized), with a numerical mean velocity of 13.20 m/s, right, raw PIV image, slight off center due to particle drift as seen in HSFC image, cropped to remove excess empty space to the right.
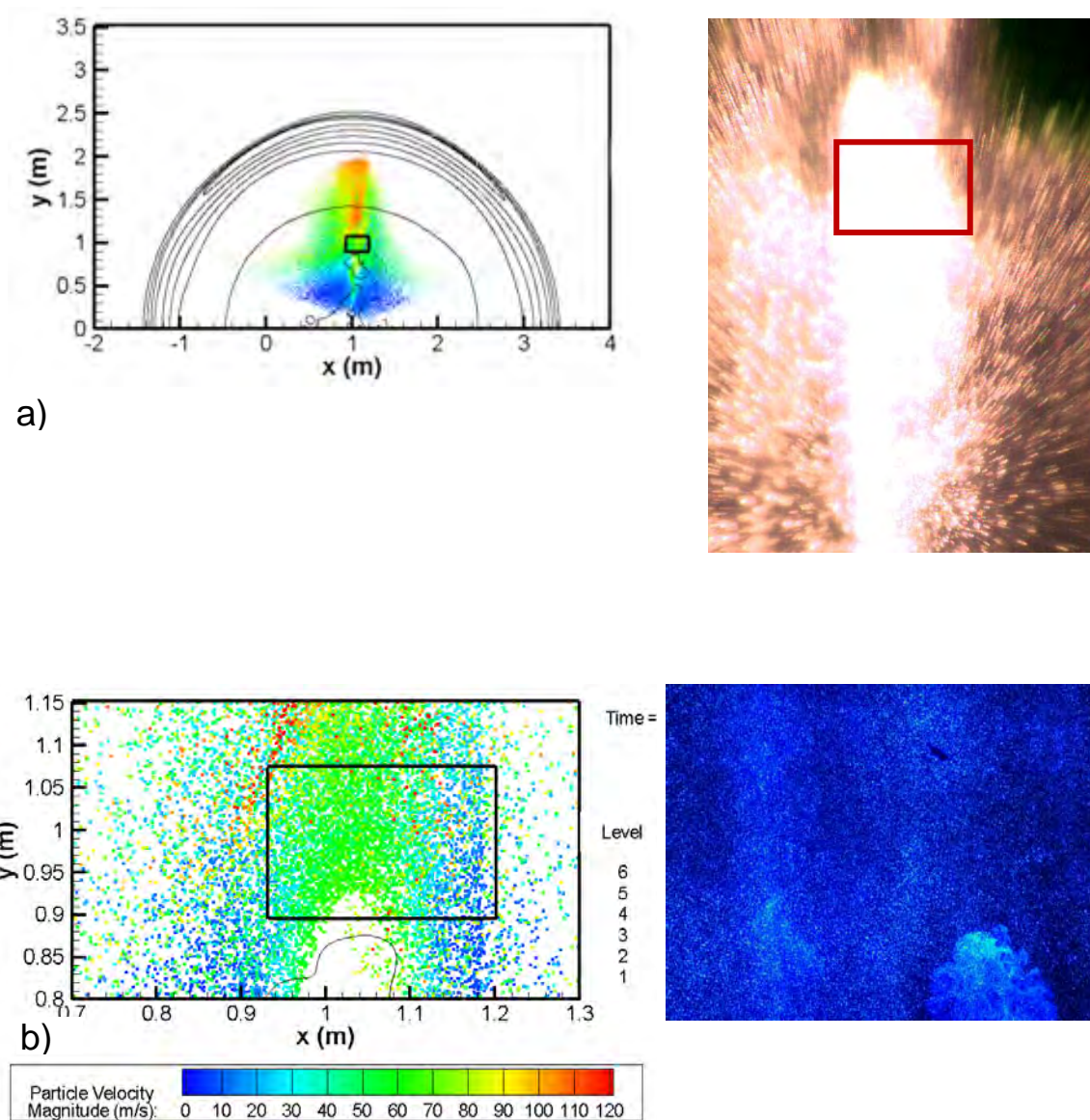
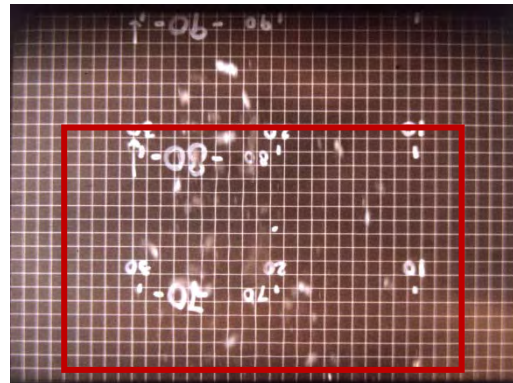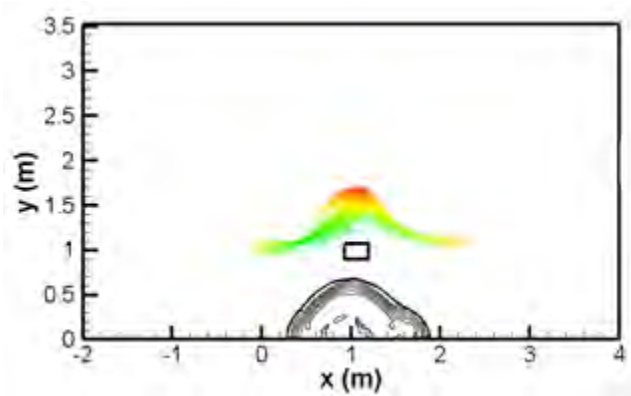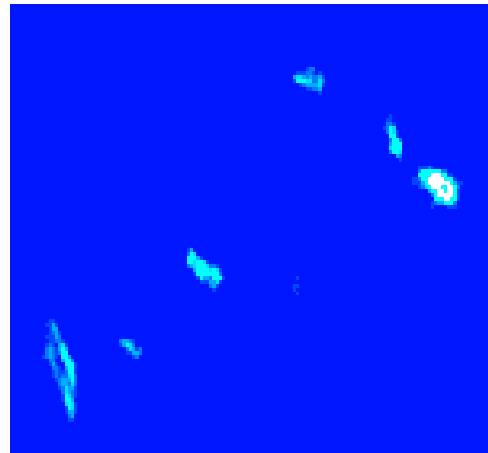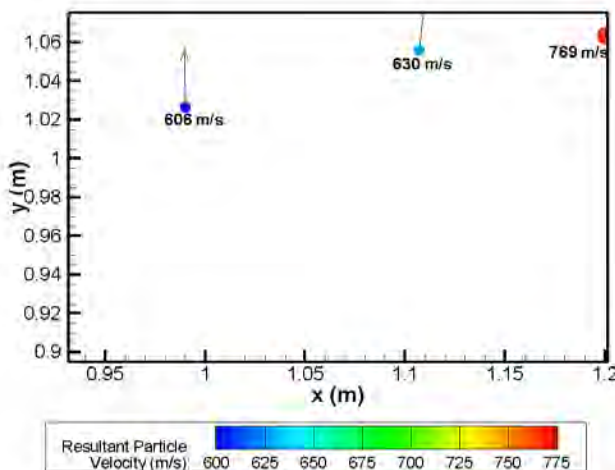Distribution A, Approved for Public Release: 96ABW-2011-0255

Figure 12. (a) Particle dispersal for W-27 HMX; right, HSFC image with estimated FOV position boxed in red (b) Close-up of particle tracking window (bottom, skip every 5th particle), with a mean numerical velocity of 55.3 m/s right, full PIV image of FOV.

Figure 13. Shock pressure and fragment velocity at 0.95 ms for HMX core and a 22.1 gram solid aluminum casing, motion is upwards to top of the frame, leading metal fragments have a prescribed distribution with Vp = 1.8 km/s; right, visual image of case break-up, using HSFC Vp = 1.5 km/s at 1 m source is set 20 cm above board (b) close-up view within the FOV, right, raw PIV image cropped to fit space and magnified, because full size image was mostly empty space with small fragment images. Differences in fragment reflectance are primarily due to angularity and orientation of particle.

DISTRIBUTION LIST
AFRL-RW-EG-TR-2011-126

*Defense Technical Info Center
8725 John J. Kingman Rd Ste 0944
Fort Belvoir VA 22060-6218

AFRL/RWME (6)
AFRL/RWOC-1 (STINFO Office)